BOUT++ nonlinear simulation for a comparative study with the measured 2D ELM structures in the KSTAR H-mode plasma

Cite as: Phys. Plasmas **26**, 052502 (2019); https://doi.org/10.1063/1.5085891
Submitted: 16 December 2018 . Accepted: 08 April 2019 . Published Online: 01 May 2019

M. Kim, H. K. Park, J. Lee, G. S. Yun, X. Q. Xu, and M. Bécoulet

Physics of Plasmas ARTICLE scitation.org/journal/php

BOUT++ nonlinear simulation for a comparative study with the measured 2D ELM structures in the KSTAR H-mode plasma

Cite as: Phys. Plasmas **26**, 052502 (2019); doi: 10.1063/1.5085891
Submitted: 16 December 2018 · Accepted: 8 April 2019 ·
Published Online: 1 May 2019

M. Kim,[1,a)] H. K. Park,[2] J. Lee,[1] G. S. Yun,[3] X. Q. Xu,[4] and M. Bécoulet[5]

AFFILIATIONS

[1]National Fusion Research Institute, Daejeon 34133, South Korea
[2]Ulsan National Institute of Science and Technology, Ulsan 44919, South Korea
[3]Pohang University of Science and Technology, Pohang, Gyeongbuk 37673, South Korea
[4]Lawrence Livermore National Laboratory, Livermore, California 94550, USA
[5]CEA, IRFM, Saint-Paul-Lez-Durance 13108, France

[a)]minwookim@nfri.re.kr

ABSTRACT

Time-dependent nonlinear simulation using the BOUT++ 3-field model is performed for a study of edge localized mode (ELM) dynamics in KSTAR H-mode plasmas. The simulated results of the ELM evolution are directly compared with the 2D ELM structures, measured by electron cyclotron emission imaging systems, from the initial growth to crash phase. The simulation results are qualitatively in good agreement with the observations. Specifically, it is notable in simulation and experiment that higher-n modes in a quasi-steady state phase evolve into lower-n modes close to the ELM-crash in time. It suggests that lower-n modes may be responsible for the onset of the crash. A postanalysis supports that nonlinear mode coupling between toroidal harmonics may drive the lower-n mode.

I. INTRODUCTION

The edge localized mode (ELM) is a critical magneto-hydrodynamic (MHD) instability driven by both the steep pressure gradient and the high current density at the edge of the H-mode plasmas. If the H-mode is adopted as an operation scenario in fusion reactors, it is necessary to regulate the ELM-crash because the heat and the particle flux from quasi-periodic ELM-crash events may cause severe damage to the internal parts of the reactor. In recent years, it has proven that the external magnetic perturbation technique is extremely effective in control of the ELM-crash in various tokamaks: KSTAR,[1–3] DIIID-D,[4] ASDEX Upgrade,[5] and JET.[6] This technique has the potential to be developed for routine control of the ELM-crash in wider plasma parameter space. A more precise understanding of the underlying physics of the ELM dynamics may lead to a predictive capability for reliable control in a variety of plasma parameters.

In KSTAR, the ELM dynamics and the crash process have been extensively studied using the electron cyclotron emission imaging (ECEI) systems.[7,8] The time evolution of the ELM-cycle was successfully visualized from the initial growth phase to the crash phase.[9] Since then, the ECEI systems have discovered a variety of dynamics of the ELMs such as the rapid change of the dominant toroidal mode number (n)[10] and simultaneous excitation of multiple modes during the inter-ELM-crash period.[11] Recently, a solitary perturbation with a low-n-number (typically $n = 1$) is observed near the onset of ELM-crash.[12] Even though the measurements provided a high-quality 2D mode structure, it was difficult to understand fundamentals of the ELM physics only based on the measured phenomenology because the dynamics of the ELM, especially the ELM-crash process, is highly nonlinear and complicated. The direct comparative study between the 2D images from observation and simulations can be a promising approach to enhance the understanding of the ELM physics because the 2D images can be strong constraints of simulation. A successful example can be the validation process of the ECEI measurement of ELM structures.[13] Here, the measured 2D structure of the saturated edge-mode in a quasi-steady state phase was directly compared with the synthetic 2D images of the ELM structure, which is the most unstable mode in the linear stability analysis, from the BOUT++ code.[14]

In this paper, a time-evolving nonlinear simulation in the BOUT++ framework is introduced for the comparison to the observed ELM dynamics from the quasi-steady state phase to the crash phase. Although there are differences in the details of the mode evolution toward the crash time, the simulation results are qualitatively in good agreement with the observations. In both simulations and experimental observations, the higher-n mode in the quasi-steady state phase evolves into the lower-n mode just before the ELM-crash time. It supports a hypothesis that the lower-n mode may be responsible for the onset of the ELM-crash. From the interpretation of the BOUT++ nonlinear simulation results, the nonlinear coupling of toroidal harmonics is the most likely explanation for the cascade to the lower-n mode.

This paper is organized as follows: In Sec. II, nonlinear simulation results from the BOUT++ are presented. In Sec. III, the nonlinear simulation results are directly compared with the time evolution of the ELM structures measured by the ECEI systems. In Sec. IV, the interpretation of ELM dynamics based on the comparative study is discussed. Finally, a summary is provided in Sec. V.

II. NONLINEAR SIMULATION OF ELMS USING BOUT++ CODE

A. Plasma equilibrium for simulation

The discharge with shot #7328 is chosen for the nonlinear simulation study since in the previous study,[13] it was used for the construction of synthetic images based on the BOUT++ linear simulation. This discharge is a typical H-mode plasma heated by ~3 MW neutral beam power, and the plasma parameters are as follows: the plasma current of $I_p = 750$ kA, the toroidal field of $B_T(R_0) = 2.25$ T, and $q_{95} \sim 5$ at the time of interest. I_p and B_T are in the same toroidal direction.

The plasma equilibrium is reconstructed using the TEQ equilibrium solver in the CORSICA package[15] based on magnetic geometry [Fig. 1(a)] calculated from EFIT code[16] and the pressure profile used in the previous study for synthetic image construction.[13] In this nonlinear simulation, the equilibrium profile of current density has been improved from the previous linear simulation by including bootstrap current component using the Sauter model.[17,18] Due to measurement errors in profile diagnostics and lack of full profile information at the pedestal, profiles may have a certain range of uncertainties. The pressure and current profiles shown in Figs. 1(b) and 1(c) are optimized by scanning the pressure profile within the constraints from the measurements and scaling the bootstrap current by a uniform factor. In the linear stability analysis using the optimized profiles, the most unstable mode number is $n = 8$, which matches well with the mode number of the coherent mode structure in ECEI observations.[13]

B. Model equations and simulation setup

Advanced models, such as the five-field[19] and the six-field[20,21] model and the coupling/splitting model for multicycle simulation,[22] have been developed in the BOUT++ framework[14] but they are not thoroughly tested for the KSTAR geometry. On the other hand, the three-field model[23] (pressure p, magnetic static potential $A_\parallel$, and vorticity ω) was tested in KSTAR H-mode discharges with various simulation settings[13] and the numerical stability of the nonlinear solution was also validated.[23] Therefore, the three-field model is used for the nonlinear study here. The following are the model equations:

$$\frac{\partial \tilde{p}}{\partial t} = -\boldsymbol{v}\cdot\nabla P + \chi_\parallel \cdot \nabla_\parallel^2 \tilde{p}, \tag{1}$$

$$\frac{\partial \tilde{A}_\parallel}{\partial t} = -\hat{\boldsymbol{b}}_0\cdot\nabla\tilde{\phi} + \frac{\eta}{\mu_0}\nabla_\perp^2\tilde{A}_\parallel - \frac{\eta_h}{\mu_0}\nabla_\perp^4\tilde{A}_\parallel, \tag{2}$$

$$\frac{\partial \tilde{\omega}}{\partial t} = -\boldsymbol{v}\cdot\nabla\tilde{\omega} + \hat{\boldsymbol{b}}_0\times\boldsymbol{\kappa}_0\cdot\nabla\tilde{p} + B_0^2\hat{\boldsymbol{b}}\cdot\nabla\left(\frac{J_\parallel}{B_0}\right) + \nu_\parallel\nabla_\parallel^2\tilde{\omega}, \tag{3}$$

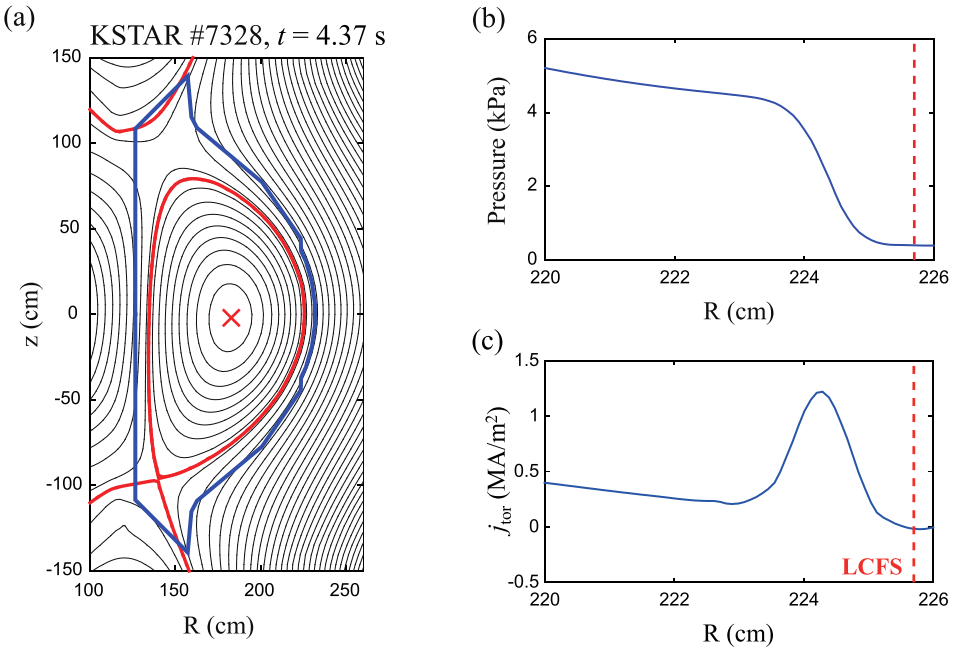

FIG. 1. (a) Flux contour of the reconstructed plasma equilibrium at $t = 4.37$ s of the KSTAR discharge #7328. Red solid line: separatrix; blue solid line: first wall. Pressure (b) and toroidal current density (c) profiles on the LFS midplane. Vertical dotted line (red): radial location of the last closed flux surface (LCFS).

$$\tilde{\omega} = \frac{n_0 M_i}{B_0}\left(\nabla_\perp^2 \tilde{\phi} + \frac{\nabla_\perp^2 \tilde{p}}{n_0 Ze}\right), \quad J_\parallel = J_{\parallel 0} - \frac{\nabla_\perp^2 \tilde{A}_\parallel}{\mu_0}, \quad \boldsymbol{v} = \frac{\hat{\boldsymbol{b}} \times \nabla_\perp \Phi}{B_0}, \tag{4}$$

$$\Phi = \Phi_0 + \tilde{\phi}, \quad P = p_0 + \tilde{p}. \tag{5}$$

The resistivity used in this BOUT++ calculation [Eq. (2)] is assumed to be uniform, for simplicity in numerical calculation, at a constant value by $\eta = 4.6 \times 10^{-7}$ Ω m, or Lundquist number is $S = 10^8$. Note that the resistivity is an order of magnitude larger compared to the Spitzer resistivity to reduce numerical artifacts and save computing resources by accelerating the growth of mode. Due to uniformity, the resistivity at the scrape-off layer (SOL), η_{SOL}, is underestimated. It is well known that η_{SOL} affects the mode growth rate: usually, the pedestal becomes more unstable as η_{SOL} increases, but not the dominant mode number at the equilibrium of interest. Additionally, *ad hoc* hyper-resistivity,[24] $\eta_h = 4.6 \times 10^{-13}$ Ω m^{-1}, is included to stimulate the radial magnetic field diffusion to reduce the CPU hours. For numerical stability, a uniform parallel viscosity $\nu_\parallel$ is included. The uniform parallel diffusivity $\chi_\parallel$, that is, effectively equivalent to the parallel thermal conductivity in the 3-field model, is 3.7×10^7 m^2 s^{-1}. The diffusivity is introduced to investigate the evolution of pedestal relaxation but exaggerated to suppress numerical artifacts. The solution is compared to cases of low and no diffusivity before they are numerically broken. All the cases show similar evolution pattern but perturbations spread over the narrower region in radial and loss of stored energy is enhanced by ∼30% with the enhanced diffusivity. The diamagnetic flow is introduced as a form of vorticity [Eq. (4)]. At the pedestal, the diamagnetic flow is strong due to the steep pressure gradient, and it can stabilize modes especially with higher-n-number.[25,26] Here, a background plasma rotation, $\boldsymbol{V}_0$ in perturbation theory, is not considered even though the toroidal rotation of the KSTAR H-mode plasma is an order of magnitude larger than that of other tokamaks.[27] In a future study, terms related to the background plasma rotation will be recovered.

A single harmonics simulation has a limit when describing the ECEI observations since the observed events, such as change of dominant n-number in the inter-ELM-crash period[10] and coexistence of multiple harmonics,[11] require more than a single mode to interpret them. The initial perturbation structure consists of multiple toroidal harmonics ($n = 1$–16) with random phases. The boundary of the radial simulation domain is from 0.8 to 1.04 in the normalized poloidal flux coordinate (ψ_{norm}). The whole torus, not a partial section of a torus, is included in the toroidal simulation domain to consider various toroidal harmonics. At the inner (outer) radial boundary, the Neumann (the Dirichlet) boundary condition is introduced as the boundary condition. Numerical methods in the present simulation are the same as those in the previous nonlinear simulation of the three-field model.[23]

C. Simulation results

1. Evolution of the edge pressure profile

Figure 2(a) illustrates the time evolution of the flux-surface averaged total pressure ($\langle p_{tot} \rangle$): the initial pressure profile ($\langle p_{tot} \rangle_{t=t_0} = p_0$) and flux-surface averaged profiles at five different simulation time steps. Here, the time step, Δt_{bout}, is 1.4×10^{-7} s (∼$0.3\tau_A$, where $\tau_A = \sqrt{\mu_0 n_0 M_i}/B_0$, μ_0 is the vacuum permeability, $n_0 = 10^{20}$ m^{-3}, M_i is the mass of hydrogen ion, and $B_0 = 1$ T). Some transport coefficients in the simulation are different from experimental numbers due to numerical reasons as described in Sec. II B. Since the quantitative approach is not matured yet to be discussed in the paper, Δt_{bout} is used as a unit of time to describe simulation results. Note that the magnetic coordinate provided in this paper is from the magnetic equilibrium geometry shown in Fig. 1(a). The initial pressure profile [black solid line in Fig. 2(a)] is relaxed as the time is evolved in the simulation and $\langle p_{tot} \rangle$ outside the separatrix [the dotted green line along the vertical axis in Fig. 2(a)] also increases. The pivot of the profile relaxation is around the steepest pressure gradient position of p_0 [$\psi_{|\nabla p|_{max}} \sim 0.954$, the dotted red line along the vertical axis in Fig. 2(a)].

Figure 2(b) shows the time evolution of the stored energy loss (ΔW_{loss}) due to the pedestal relaxation which can be estimated using

$$\Delta W_{loss} \propto \int_{\psi_{in}}^{\psi_{out}} d\psi \int\int d\theta d\phi (p_{tot} - p_0)\sqrt{g}, \tag{6}$$

where p_0 is the equilibrium pressure profile, $p_{tot} - p_0$ is equivalent to the pressure perturbation ($\tilde{p}$), and $g = J^2$ where J is the Jacobian. Here, ΔW_{loss} is used to represent a relative magnitude of pedestal relaxation

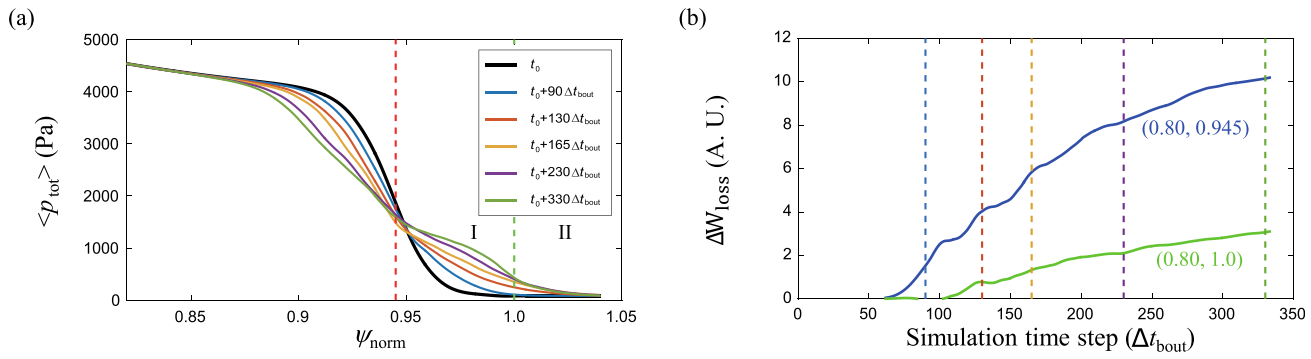

FIG. 2. (a) Equilibrium pressure profile (black solid line) and flux-surface averaged total pressure profiles at five different BOUT++ simulation time steps in normalized poloidal flux coordinate. Red dotted line: the position of the steepest pressure gradient; green dotted line: separatrix. (b) Time evolution of the stored energy loss is shown. Integration boundary is from the inner simulation boundary to the steepest pressure gradient (blue solid line) and the separatrix (green solid line). The color of each vertical dotted line corresponds to that of the $\langle p_{tot} \rangle$ profile in (a) at five different simulation time steps.

because the simulation is qualitatively verified. ψ_{in} is fixed as ψ_{norm} at the inner boundary of the simulation domain. ψ_{out} has two cases: (1) $\psi_{out} = \psi_{|\nabla p|_{max}}$ [blue line in Fig. 2(b)], (2) $\psi_{out} = 1.0$, or ψ_{norm} at separatrix [green line in Fig. 2(b)]. Vertical dotted lines indicate the time point when the $\langle p_{tot} \rangle$ profiles are obtained in Fig. 2(a). In both cases, the energy loss increases in time; however, the speed of loss gradually decreases especially after $\sim 220\Delta t_{bout}$. The energy loss of the case (1) is about 4 times larger than that of the case (2). The difference between the two curves corresponds to the increase in the stored energy at region I labeled in Fig. 2(a). In Fig. 2(a), it is clear that the increase in $\langle p_{tot} \rangle$ in region I is larger than that in region II. The time evolution of $\langle p_{tot} \rangle$ profile is consistent with that of the stored energy loss.

2. Spectra of toroidal mode number

A spectrum of the toroidal mode number (n) is obtained to investigate the time evolution of the toroidal harmonics which are set as initial perturbation structures. Figure 3(a) shows the integrated power spectra along the radial direction on the low field side (LFS) midplane at the time when the $\langle p_{tot} \rangle$ profile is calculated in Fig. 2(a). The spectral power of the $n = 0$ component increases in time due to the mean value drift of $\tilde{p}$ which causes the relaxation of $\langle p_{tot} \rangle$ profiles.

On the LFS midplane, the evolution of toroidal mode spectrum is shown in Figs. 3(b)–3(f) where the $n = 0$ component is not included to study other components. At $90\Delta t_{bout}$ [Fig. 3(b)], the $n = 8$ is the dominant structure as designed at the step of plasma equilibrium optimization. The dominant mode sustains until $165\Delta t_{bout}$ [Figs. 3(c) and 3(d)]. At $230\Delta t_{bout}$ [Fig. 3(e)], the dominant mode is diminished, and broadband spectra appear. At $330\Delta t_{bout}$ [Fig. 3(f)], the $n = 4$ mode becomes the dominant mode at $\psi_{norm} \sim 0.92$ ($\psi_{norm} \sim 0.945$ for the $n = 8$ mode) but it is not clear as much as the $n = 8$ mode in earlier times.

3. Mode structures in the poloidal or toroidal view

In Fig. 4, the pressure perturbation ($\tilde{p}$) structures corresponding to five different time steps in Fig. 2(a) at the LFS edge are illustrated on the poloidal plane where the view window is chosen to match with the ECEI. It is more efficient to compare them to the measured images from ECEI. The flux-surface averaged part of perturbation ($\langle \tilde{p} \rangle$, or

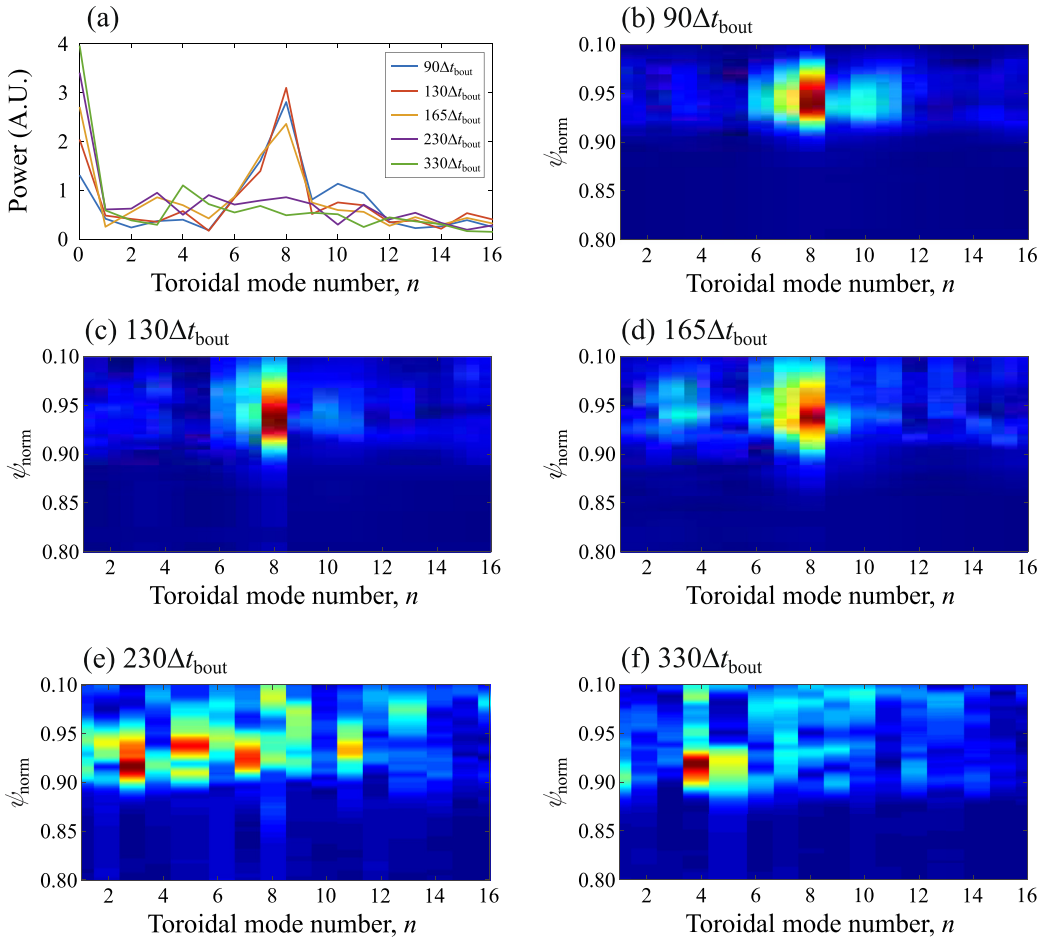

FIG. 3. (a) Radially integrated toroidal mode number spectrum of the pressure perturbation on LFS midplane. Toroidal mode number spectra on LFS midplane at $90\Delta t_{bout}$ (b), $130\Delta t_{bout}$ (c), $165\Delta t_{bout}$ (d), $230\Delta t_{bout}$ (e), and $330\Delta t_{bout}$ (f). $n = 0$ component is excluded in (b)–(f) because it overwhelms other components.

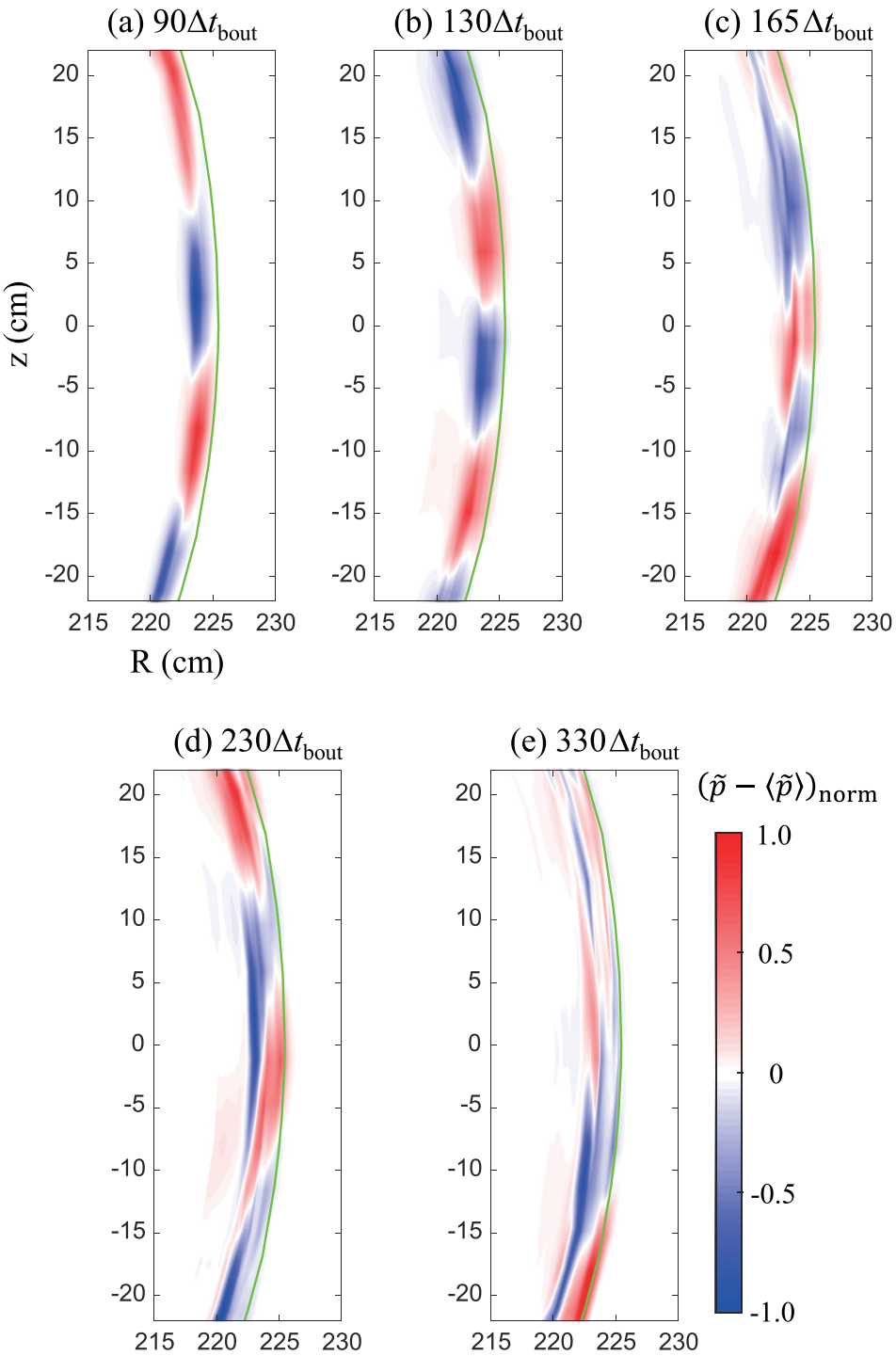

FIG. 4. 2D slices (at five simulation time steps described in Fig. 2) of the 3D pressure perturbation structure on the poloidal plane at LFS edge. Each slice is normalized by its absolute maximum of $\tilde{p} - \langle\tilde{p}\rangle$. Green solid line: LCFS from the initial magnetic geometry illustrated in Fig. 1(a).

$n = 0$ component) is excluded for investigation of other components in detail and $\tilde{p} - \langle\tilde{p}\rangle$ is normalized by its absolute maximum. It is effectively equivalent to the 2D fluctuation in ECEI; however, in the ECEI data process, the signal is normalized by the time-averaged value at the time of interest after subtracting it from original data: $(T - \langle T\rangle_t)/\langle T\rangle_t$. Note that the initial perturbations do not settle as an eigenmode structure before $\sim 90\Delta t_{\text{bout}}$. As shown in n-number spectra (Fig. 3), $n = 8$ mode is the dominant component until $\sim 165\Delta t_{\text{bout}}$

[Figs. 4(a)–4(c)]. However, at $165\Delta t_{bout}$, the perturbation structure is not clear as much as in previous time [Fig. 4(c)]. Mode structures in Figs. 4(d) and 4(e) correspond to the time of broadband spectrum [Fig. 3(e)] and dominant $n = 4$ component [Fig. 3(f)] in spectral analysis, respectively. However, it is not clear that mode structures in Figs. 4(d) and 4(e) match with the spectral analysis results.

Figure 5 shows the perturbation structures on the LFS midplane along the toroidal angle to confirm the results shown in Figs. 3(e) and 3(f). At $90\Delta t_{bout}$ [Fig. 5(a)] for a reference case, a clear symmetric $n = 8$ structure appears. A small variation in the mode structure is due to the harmonics as shown in Figs. 3(a) and 3(b). The fact that the $n = 8$ mode is still the dominant component at $165\Delta t_{bout}$ [Fig. 5(b)] is consistent with the spectral analysis shown in Fig. 3(d). As shown in the mode spectrum at $165\Delta t_{bout}$ [Fig. 3(d)], the spectral power ratio of other components to the $n = 8$ mode increases compared to the previous time. This increase in other mode amplitudes, in return, produces distortion of the mode structure projected onto the toroidal plane. At $230\Delta t_{bout}$ and $330\Delta t_{bout}$, the perturbation structures in the toroidal view are consistent with the previous spectral analysis results. At $230\Delta t_{bout}$ [Fig. 5(c)], the mode structure becomes difficult to define any specific mode number. At $330\Delta t_{bout}$ [Fig. 5(d)], the clarity of the mode structure is not as good as the $n = 8$ mode structure shown at $90\Delta t_{bout}$, but the presence of the $n = 4$ mode is apparent even though it is irregular in the toroidal view.

As shown in Figs. 5(b)–5(d), the perturbations are expelled to the scrape-off layer (SOL). The SOL region can influence the ELM dynamics like the onset and size of the crash. In particular, during the crash, the main plasma is connected to the SOL and divertor through open field lines. Therefore, the level of recycling and particle flow in the SOL can be significantly changed. For the ELM simulations to include SOL dynamics, it is necessary to introduce a self-consistent SOL model and appropriate boundary condition, such as a sheath boundary condition. However, those are not fully implemented in the present simulation because the main subject of this paper is the time evolution of the mode structure inside the separatrix which can be directly compared to the structures visualized by the ECEI systems. The current boundary condition at the outer radial boundary (the Dirichlet condition) works properly without critical distortion of the perturbation structure, particularly toroidal mode spectra in the time window of interest. Even though the SOL region is not the main focus here, the simulation domain contains a part of SOL since the X-point is included in the domain; in the LFS midplane, the simulation domain outside the separatrix, $\psi_{norm} = [1.0, 1.04]$, corresponds to ~1 cm in real dimension, and the gap between the separatrix and plasma facing components is ~5 cm. Note that the edge stability can be different whether the X-point is introduced in the domain or not.[28]

III. A COMPARATIVE STUDY WITH THE ECEI OBSERVATIONS

The ECEI systems successfully visualize the evolution of the ELM structure close to and during the ELM-crash.[9] However, a violent change of the edge pedestal due to the crash makes it complicated to model the ECEI 2D imaging data. The comparative study with the simulation results prior to the ELM-crash time can guide us to have a comprehensive understanding of the dynamics of ELM and ELM-

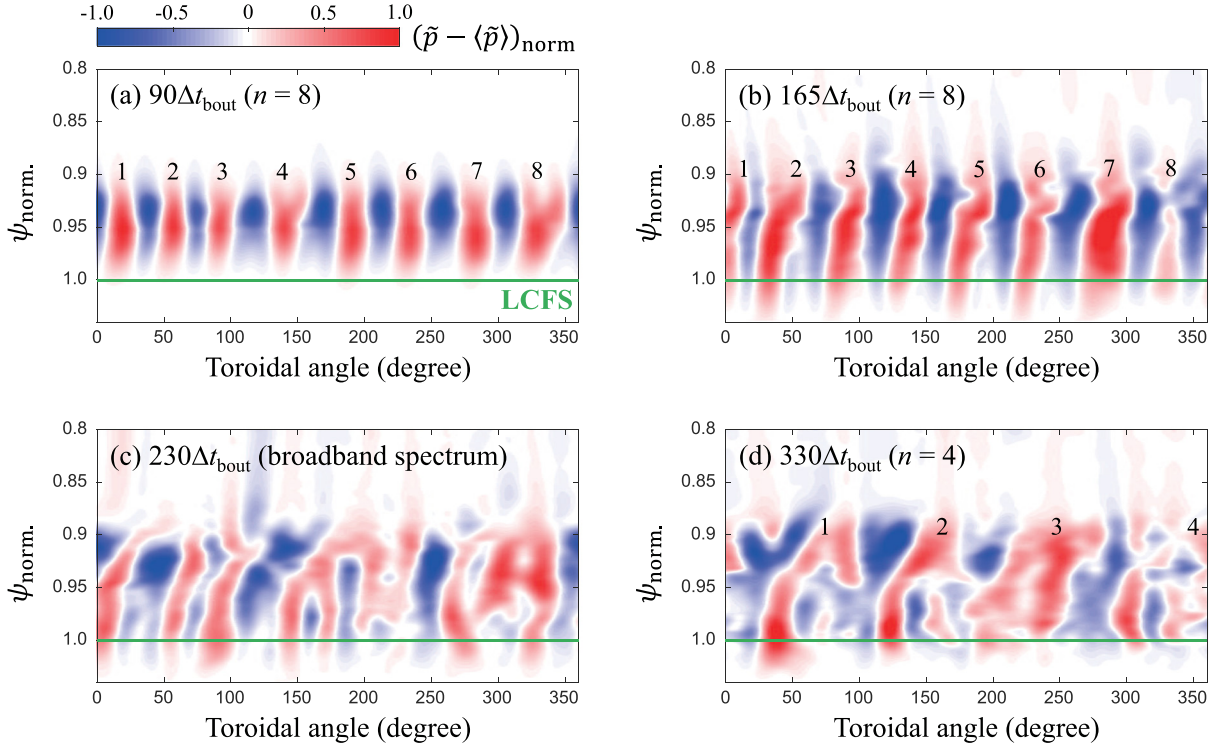

FIG. 5. Pressure perturbation structure along the toroidal angle on the LFS midplane. Each frame is normalized by its absolute maximum of $\tilde{p} - \langle\tilde{p}\rangle$ at $90\Delta t_{bout}$ (a), $165\Delta t_{bout}$ (b), $230\Delta t_{bout}$ (c), and $330\Delta t_{bout}$ (d).

crash. As described in Sec. II, the simulation for quantitative comparison is beyond the scope of this paper. The observations are compared qualitatively with the simulation results with attention on evolution of the edge structures.

A. ELM dynamics observed by ECEI

Figure 6 shows imaging data from the KSTAR ECEI systems[7,8] during one ELM-cycle at the time of interest when the plasma equilibrium in Sec. II A is reconstructed. In Fig. 6(a), peaks in D_α time trace (red line) indicate the timing of ELM-crash. The raw signal of single ECEI antenna [black line, channel 14–3, a cross mark in Fig. 6(b)] provides a change of radiation temperature (T_{rad}) in the pedestal region, but it cannot describe the evolution of the edge structure. 2D images are obtained at the time as indicated by the vertical green lines in Fig. 6(a) when the edge structure varies.

As the pedestal builds up after the ELM-crash, $n = 8$ becomes dominant at $t \sim 4.36$ s and sustains for ~15 ms [Fig. 6(b)] which is nearly a quasi-steady state phase. In KSTAR, the modes in the quasi-steady state phase are often observed, and they usually sustain for ~100 μs–10 ms.[9,10,13] Note that the plasma equilibrium used in the simulation is obtained at the time when the following two conditions are simultaneously satisfied; profile diagnostics data are available, and it is the closest time to the ELM-crash in the quasi-steady state phase. Then, the mode almost vanishes transiently in the view window of the ECEI system [Fig. 6(c)] during ~100 μs and reappears with a lower-n-number, $n \sim 6$, in the relatively irregular pattern in poloidal [Fig. 6(d)]. Soon after the reappearance of the low-n mode, a pedestal collapses, and transport of heat and particle occurs crossing the separatrix [Fig. 6(e)]. During the ELM-crash, the region outside the separatrix in the ECE-images becomes difficult to interpret since the down-shifted emission spectra usually saturate the ECEI receivers.

The above observation is a typical evolution pattern of the pedestal in KSTAR ELMy H-mode plasmas as described in Ref. 9, but variations also exist. The ECEI systems sometimes do not capture the transient and reappearing phase or both of them. If the duration of a particular phase is shorter than the time resolution of the systems or the reappearing mode is the spatially localized structure, the ECEI systems cannot capture the phase. Recently, a different type of pedestal evolution is observed; a low-n mode (typically $n = 1$), called a solitary perturbation, appears within ~100 μs before the ELM-crash with the coherent mode structure existing.[12]

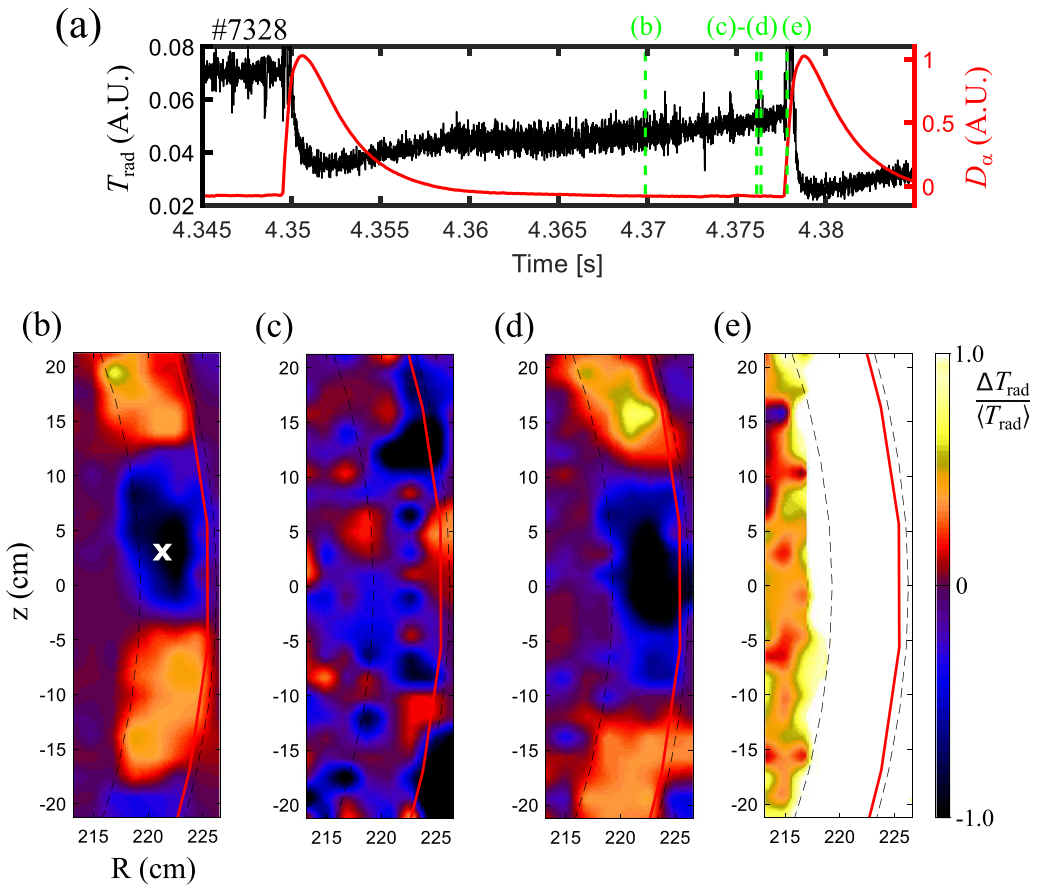

FIG. 6. (a) Time trace of D_α and raw signal of ECEI single channel [#14-3, marked in (b)] during one cycle of ELM dynamics. 2D imaging data from ECEI system in the quasi-steady state (b), the transient (c), the reappearance (d), and the crash phase (e).

B. Comparison of mode evolution using synthetic images

For direct comparison to the observed ELM dynamics, the BOUT++ nonlinear simulation results illustrated in Fig. 4 are converted into synthetic images, as shown in Fig. 7, using the synthetic diagnostics of ECEI.[13,29] Electron density and temperature distributions for the synthetic diagnostics are extracted from the pressure in the simulation using the relations $p = p_e + p_i$ and $p_e = n_e + T_e$. Fluctuations in the synthetic images are represented in $\Delta T_{rad}/\langle T_{rad}\rangle$ which is the form of the measured ECE-images, where $\langle T_{rad}\rangle$ is a time average of radiation temperature. In the synthetic diagnostics, $\langle T_{rad}\rangle$ is obtained from $\langle p_{tot}\rangle$ at each simulation time step shown in Fig. 2(a), or $n = 0$ is introduced as an averaging part. It is assumed that $T_e = T_i$ and density is constant in time. The recent forward modeling of electron cyclotron emission (ECE)[30] indicates that n_e fluctuation can mainly contribute to intensity fluctuation of the ECE at the pedestal region where the plasma is optically thin or gray, but the effect on the shape of the mode structure is insignificant. Because the subject of the comparative study is comparing the evolution pattern of the edge perturbation structure, the above assumptions are valid.

The dominant structures, coherent $n = 8$ mode, are illustrated in Figs. 7(a) and 7(b). The distortion of the mode structure at $165\Delta t_{bout}$ [Fig. 7(c)] is consistent with the spectral analysis result [Fig. 3(d)] and the projected structure onto a toroidal plane [Fig. 5(b)]. The emission outside the separatrix is mixed with the down-shifted emission from inside, and the signal level of outside channels is usually comparable to the thermal noise of electronics of the ECEI systems.[13,29] It is not worth to interpret the details of the signal outside the separatrix.

At $230\Delta t_{bout}$ [Fig. 7(d)], the mode structure appears despite the broadband spectra in the spectral analysis [Fig. 3(e)]. It is not similar

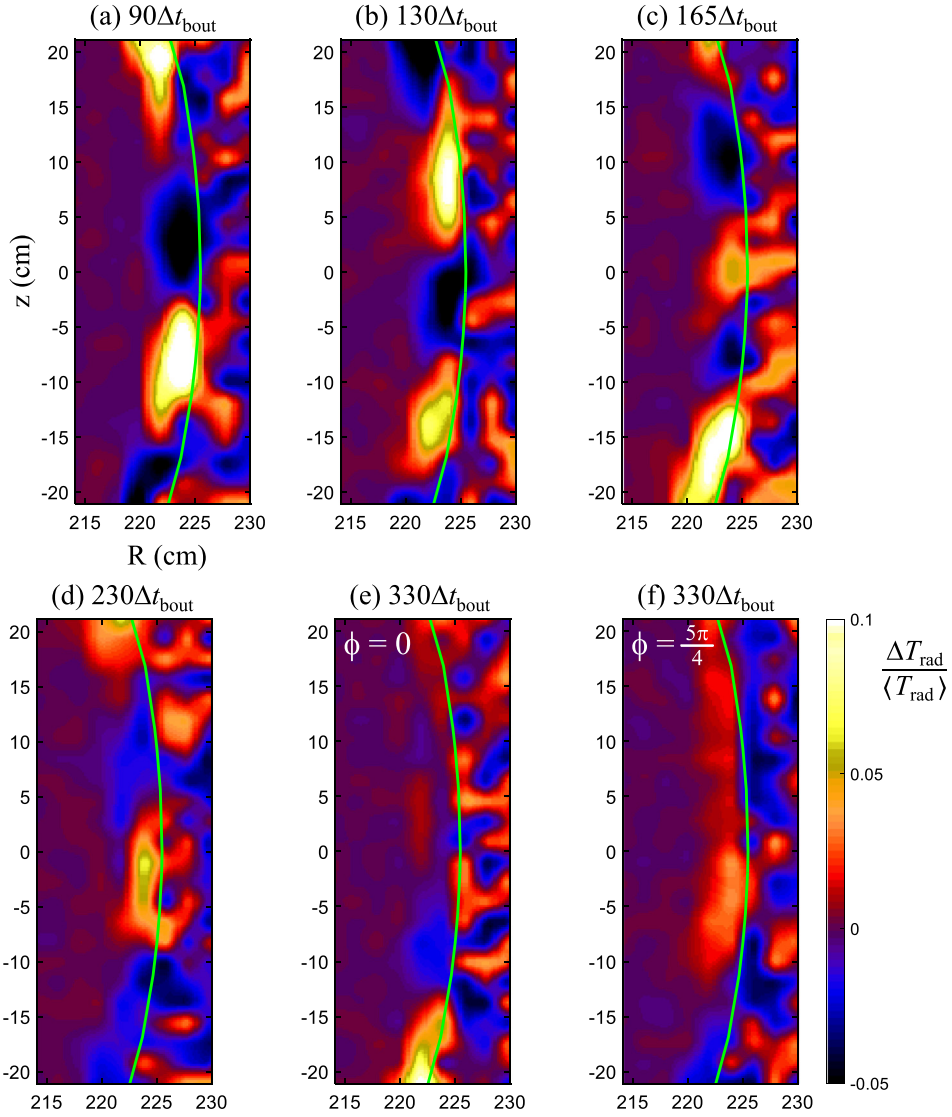

FIG. 7. Synthetic images are constructed based on the nonlinear simulation result illustrated in Fig. 4. (e) and (f) are at the same simulation time step but different toroidal positions; $\phi = 0$ and $\phi = 5\pi/4$, respectively.

to the observation in the transient phase [Figs. 6(c) and 3(c) in Ref. 9]. In the spectrogram at the broadband phase [Fig. 3(e)], some harmonics, for example, $n = 3$, 5, 7, and 11, have stronger spectral power amplitude. The superposition of them can produce a specific mode structure with some distortion as shown in Figs. 4(d) and 7(d) although the spectrum becomes broad; depending on the relative phase of the harmonics in a simulation, the modes at broadband phase can have various mode patterns. If the mode is spatially localized, it is possible that the ECEI system cannot capture any perturbation during a short period of the transient phase. Because, in a real situation, harmonics higher than $n = 16$ ($n = 1$–16 in the BOUT++ simulation) can exist, the transient phase can be more likely to appear. However, the conditions are too strict to explain the transient phase observed frequently.

At $330\Delta t_{\mathrm{bout}}$ [Fig. 7(e)], the perturbation structure is not a coherent mode pattern, and it is irregular in the poloidal direction. The mode structures in the toroidal view [Fig. 5(d)] confirm the transition of the dominant mode number to the lower-n-number. However, it is not evident in the synthetic images which may be due to the irregular poloidal mode pattern and finite spatial resolution of the ECEI system. At different toroidal locations [$\phi = 5\pi/4$, Fig. 7(f)], a synthetic image confirms the increase in the poloidal mode size derived by the lower-n mode dominance (here, $n = 4$). Although the dominant mode number is different from that in the observation [Fig. 6(d), $n \sim 6$], the simulation reproduces the decreasing trend of the n-number.

Consequently, the simulation results are qualitatively in reasonably good agreement with the observations although differences do exist in details of mode evolution. Specifically, the BOUT++ simulation results show that the broadening of the mode number spectra and the change in the dominant mode number appear in order. Moreover, the perturbation pattern is relatively irregular when the dominant mode number becomes lower. The differences in images from the simulation can be contributed from the uncertainty in initial equilibrium profiles (even though it gives $n = 8$ as the most unstable mode), the parameters of transport, and the number of harmonics included in the simulation.

IV DISCUSSION

A. Low-n mode excitation before ELM-crash

In both BOUT++ nonlinear simulation and the ECEI observation, the low-n mode (a mode with lower-n-number compared to the mode in quasi-steady state phase) appears before the onset of ELM-crash. Another experimental example is that, on TCV, a magnetic perturbation of low-n-number ($n = 1$ is most frequent) is measured by the magnetic probe close to the ELM-crash in time.[31]

The nonlinear simulation by JOREK using the same plasma equilibrium mentioned in Sec. II A shows a similar trend of mode evolution.[32] The $n = 8$ mode is the dominant component at the initial phase. As it approaches the ELM-crash event, the magnetic energy contained in each of harmonics becomes comparable (Fig. 16 in Ref. 32). Specifically, the lower toroidal modes ($n = 1$–3), which are stable in the initial phase, are excited. However, they do not become the dominant modes. Even though two codes share the same plasma equilibrium, several factors are not identical, for example, the geometry of the simulation mesh, the total number of harmonics taken into consideration ($n = 1$–8 in JOREK), and the transport parameters (such as resistivity, viscosity, and conductivity). Note that each code is optimized in different operation windows so that each code is numerically stable and efficiently converged. In principle, it is necessary to use the same initial conditions for a fair comparison, and cross-validation of the code is one of the future objectives. In both codes, the diamagnetic stabilization effect is included.

It may not be conclusive, but low-n modes play a definite role in a triggering mechanism of the ELM-crash. To prove this hypothesis, it is necessary to investigate the connection between the low-n mode and sudden pedestal relaxation. Here, the mechanism driving the low-n modes is discussed as a first step.

B. Mechanism driving low-n modes

Since the $\langle p_{\mathrm{tot}} \rangle$ profiles are evolved in time as shown in Fig. 2(a), stability conditions of the edge can be changed. If the pedestal conditions become favorable to the peeling mode, the low-n mode structure can appear because a peeling mode usually has a low-n mode number.[33] At the initial equilibrium profiles ($n = 8$) and $330\Delta t_{\mathrm{bout}}$ [$n \sim 4$ appears, Figs. 3(f) and 5(d)], growth rate spectra are obtained by linear stability analysis of BOUT++ using the same simulation conditions described at Sec. II B. As the decreased pressure gradient weakens the diamagnetic stabilizing effect, the peak of growth rate spectrum is changed from $n = 8$ (at the initial time, black curve in Fig. 8) to $n = 14$ (at $330\Delta t_{\mathrm{bout}}$, green). Additionally, the relaxation of the pedestal reduces the free energy driven by the pressure gradient and, consequently, the peak value of the growth rate is decreased. Although the linear stability analysis is consistent with the evolution of pedestal profiles, it cannot explain the appearance of the low-n mode in the nonlinear simulation.

Another possible driving mechanism is a nonlinear process among modes. Experimental examples of excitation of multiple harmonics, introduced at the introduction, support this conjecture; the amplitude of the visualized mode structure is modulated like beating signals,[11] and two harmonics coexist in some cases of the rapid change in the dominant n-number during the inter-ELM-crash period.[10] Moreover, the results of linear stability analysis (Fig. 8) show that the harmonics adjacent to the dominant mode has a finite growth rate comparable to the growth rate of the dominant mode. Figure 9 shows the evolution of the spectral power of the pressure perturbation. The spectral power of each harmonic is integrated over the plasma volume

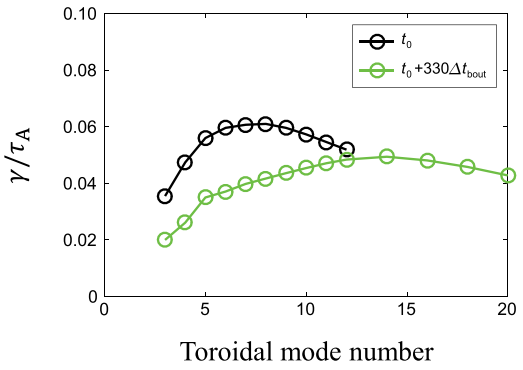

FIG. 8. Results of linear stability analysis using equilibria at t_0 (black) and $330\Delta t_{\mathrm{bout}}$ (green). The dominant mode number is shifted to a higher number ($n = 8$ to ~14).

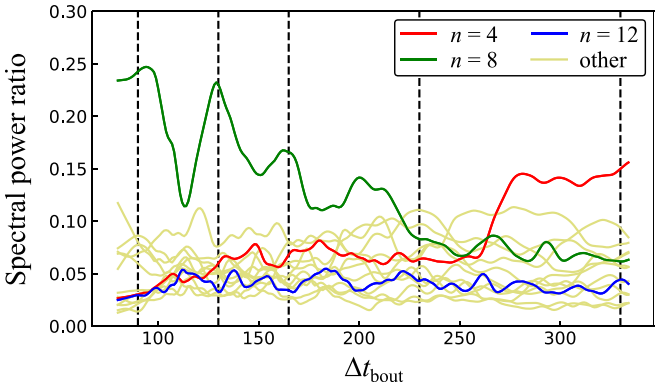

FIG. 9. Time trace of the spectral power ratio of $n = 1$–16 pressure perturbation. Volume-integrated spectral power of each harmonic is normalized by the integrated spectral power of entire harmonics.

enclosed by the inner simulation boundary and the separatrix, and then normalized by volume-integrated total spectral power. Vertical dotted lines indicate the times when the synthetic images (Fig. 7) are constructed. It is clear that the spectral power of the $n = 8$ mode (initially dominant mode) decreases and that of the $n = 4$ mode (low-n mode) increases after the broadband phase ($\Delta t_{bout} \sim 230$–255) where the spectral power of harmonics becomes comparable. It seems that the energy contained in the higher-n mode at the quasi-steady state phase is redistributed into the lower-n mode by the nonlinear mode interaction through the broadband spectra phase. However, if the low-n mode is driven by the nonlinear mode interaction, following questions should be resolved to understand the fundamentals: how contained energy of a particular harmonics transfers to other harmonics and why energy transfer is favorable to the lower-n-number.

The energy in the $n = 8$ mode, initially dominant mode, can transfer to the $n = 4$ mode, low-n mode, by coupling with the $n = 12$ mode which satisfies the condition $n_i = n_j \pm n_k$ for $i, j, k = 1, 2, \ldots, 16$ where n_i, n_j, and n_k are the harmonic number. However, it is necessary to consider the coupling of other modes since the $n = 4$ mode appears after broadband phase where the energy of the $n = 8$ mode is already redistributed to several modes. Due to complexity, it is not trivial to quantify the energy transfer rate and direction. It is certainly beneficial to implement a diagnostic model for energy transfer in a simulation and design systematic postanalysis process. However, it is one of the important topics in a follow-up study including the relationship between low-n modes and the crash triggering.

V. SUMMARY

The nonlinear simulation results from BOUT++ code are directly compared with the 2D images of the ELM dynamics, especially near the ELM-crash time, measured by the ECEI systems. The observed evolution of the mode structure from initial growth to the crash is not perfectly reproduced in the simulations. However, the simulation results qualitatively agree with the observed nonlinear ELM dynamics. The broadening of mode number spectra in the BOUT++ is probably closely related to the transient phase in the observations. After the broadband spectra, the n-number of the dominant mode becomes lower compared to the initial one as in the ECEI observation just before the ELM-crash. Other examples of similar mode evolution trends exist: the analysis results of magnetic signals in TCV and the JOREK multimode simulation for KSTAR, which shares the same plasma equilibrium used in the BOUT++ simulation. From the experiments and the simulations, it is reasonable to conclude that the low-n mode may play a role in triggering the ELM-crash. It seems that nonlinear interactions of modes drive the low-n mode, but further investigation is required to understand the underlying physics of low-n mode appearance and ELM-crash triggering.

ACKNOWLEDGMENTS

This work was supported by the National Research Foundation (NRF) of Korea under Grant No. NRF-2014M1A7A1A03029865 and the Korea Ministry of Science and ICT under NFRI R&D programs (NFRI-EN1801-9).

REFERENCES

[1]Y. M. Jeon, J.-K. Park, S. W. Yoon, W. H. Ko, S. G. Lee, K. D. Lee, G. S. Yun, Y. U. Nam, W. C. Kim, J.-G. Kwak *et al.*, Phys. Rev. Lett. **109**, 035004 (2012).
[2]J. Lee, G. S. Yun, M. J. Choi, J.-M. Kwon, Y.-M. Jeon, W. Lee, N. C. Luhmann, Jr., and H. K. Park, Phys. Rev. Lett. **117**, 075001 (2016).
[3]Y. In, J.-K. Park, Y. M. Jeon, J. Kim, G. Y. Park, J.-W. Ahn, A. Loarte, W. H. Ko, H. H. Lee, J. W. Yoo *et al.*, Nucl. Fusion **57**, 116054 (2017).
[4]C. Paz-Soldan, R. Nazikian, S. R. Haskey, N. C. Logan, E. Strait, N. M. Ferraro, J. M. Hanson, J. D. King, M. J. Lanctot, R. A. Moyer *et al.*, Phys. Rev. Lett. **114**, 105001 (2015).
[5]W. Suttrop, T. Eich, J. C. Fuchs, S. Günter, A. Janzer, A. Herrmann, A. Kallenbach, P. T. Lang, T. Lunt *et al.*, Phys. Rev. Lett. **106**, 225004 (2011).
[6]Y. Liang, P. Lomas, I. Nunes, M. N. A. Gryaznevich, M. Beurskens, S. Brezinsek, J. W. Coenen, P. Denner, Th. Eich, L. Frassinetti *et al.*, Nucl. Fusion **53**, 073036 (2013).
[7]G. S. Yun, W. Lee, M. J. Choi, J. B. Kim, H. K. Park, C. W. Domier, B. Tobias, T. Liang, X. Kong, N. C. Luhmann *et al.*, Rev. Sci. Instrum. **81**, 10D930 (2010).
[8]G. S. Yun, W. Lee, M. J. Choi, J. B. Lee, M. Kim, J. Leem, Y. Nam, G. H. Choe, H. K. Park, H. Park *et al.*, Rev. Sci. Instrum. **85**, 11D820 (2014).
[9]G. S. Yun, W. Lee, M. J. Choi, J. Lee, H. K. Park, C. W. Domier, N. C. Luhmann, Jr., B. Tobias, A. J. H. Donné, J. H. Lee *et al.*, Phys. Plasmas **19**, 056114 (2012).
[10]J. E. Lee, G. S. Yun, M. Kim, J. Lee, W. Lee, H. K. Park, C. W. Domier, N. C. Luhmann, Jr., W. H. Ko *et al.*, Nucl. Fusion **55**, 113035 (2015).
[11]M. Kim, J. Lee, H. K. Park, G. S. Yun, W. Lee, C. W. Domier, N. C. Luhmann, Jr., *et al.*, Nucl. Fusion **55**, 073001 (2015).
[12]J. E. Lee, G. S. Yun, W. Lee, M. Kim, M. H. Choi, J. Lee, M. Kim, H. K. Park, J. G. Bak, W. H. Ko *et al.*, Sci. Rep. **7**, 45075 (2017).
[13]M. Kim, M. J. Choi, J. Lee, G. S. Yun, W. Lee, H. K. Park, C. W. Domier, N. C. Luhmann, Jr., X. Q. Xu, KSTAR Team *et al.*, Nucl. Fusion **54**, 093004 (2014).
[14]B. D. Dudson, M. V. Umansky, X. Q. Xu, P. B. Snyder, and H. R. Wilson, Comput. Phys. Commun. **180**, 1467 (2009).
[15]T. A. Casper, W. H. Meyer, L. D. Pearlstein, and A. Portone, Fusion Eng. Des. **83**, 552 (2008).
[16]L. L. Lao, H. St. John, R. D. Stambaugh, A. G. Kellman, and W. Pfeiffer, Nucl. Fusion **25**, 1611 (1985).
[17]O. Sauter, C. Angioni, and Y. R. Lin-Liu, Phys. Plasmas **6**, 2834 (1999).
[18]O. Sauter, C. Angioni, and Y. R. Lin-Liu, Phys. Plasmas **9**, 5140 (2002).
[19]T. Y. Xia and X. Q. Xu, Phys. Plasmas **20**, 052102 (2013).
[20]T. Y. Xia, X. Q. Xu, and P. W. Xi, Nucl. Fusion **53**, 073009 (2013).
[21]T. Y. Xia and X. Q. Xu, Nucl. Fusion **55**, 113030 (2015).
[22]X. Xu, T. Xia, N. Yan, Z. Liu, D. Kong, A. Diallo, R. Groebner, A. Hubbard, and J. Hughes, Phys. Plasmas **23**, 055901 (2016).
[23]X. Q. Xu, B. D. Dudson, P. B. Snyder, M. V. Umansky, H. R. Wilson, and T. Casper, Nucl. Fusion **51**, 103040 (2011).
[24]P. K. Kaw, E. J. Valeo, and P. H. Rutherford, Phys. Rev. Lett. **43**, 1398 (1979).

[25]W. Tang, R. L. Dewar, and J. Manickam, Nucl. Fusion **22**, 1079 (1982).
[26]G. Huysmans, Plasma Phys. Controlled Fusion **47**, B165 (2005).
[27]S. H. Ko, J. M. Kwon, W. H. Ko, S. S. Kim, H. Jhang, and L. Terzolo, Phys. Plasmas **23**, 062502 (2016).
[28]S. Saarelma, O. Kwon, A. Kirk, MAST Team *et al.*, Plasma Phys. Controlled Fusion **53**, 025011 (2011).
[29]M. J. Choi, G. S. Yun, W. Lee, H. K. Park, Y.-S. Park, S. A. Sabbagh, K. J. Gibson, C. Bowman, C. W. Domier, N. C. Luhmann, Jr., *et al.*, Nucl. Fusion **54**, 083010 (2014).
[30]B. Vanovac, E. Wolfrum, S. Denk, F. Mink, F. Laggner, G. Birkenmeier, M. Willensdorfer, E. Viezzer, M. Hoelzl, S. Freethy *et al.*, Plasma Phys. Controlled Fusion **60**, 045002 (2018).
[31]R. P. Wenninger, H. Reimerdes, O. Sauter, and H. Zohm, Nucl. Fusion **53**, 113004 (2013).
[32]M. Bécoulet, M. Kim, G. Yun, S. Pamela, J. Morales, X. Garbet, G. T. A. Huijsmans, C. Passeron, O. Février, M. Hoelzl *et al.*, Nucl. Fusion **57**, 116059 (2017).
[33]S. Saarelma, A. Alfier, M. N. A. Beurskens, R. Coelho, H. R. Koslowski, Y. Liang, I. Nunes *et al.*, Plasma Phys. Controlled Fusion **51**, 035001 (2009).